EXPERIMENTAL ANALYSIS OF POROSITY FORMATION IN LASER-ASSISTED POWDER DEPOSITION PROCESS

L. Wang[1], P. Pratt[2], S.D. Felicelli[1,2], H. El Kadiri[1,2], J.T. Berry[1,2], P.T. Wang[1,2], M.F. Horstemeyer[1,2]

[1]Center for Advanced Vehicular Systems, Mississippi State University, Mississippi State, MS 39762, USA

[2]Mechanical Engineering Department, Mississippi State University, Mississippi State, MS 39762, USA

Key Words: Laser-assisted powder deposition, porosity, LENS, laser engineered net shaping

Abstract

Pore formation remains a concern in the area of rapid manufacturing by the Laser Engineered Net Shaping (LENS) process. Results usually conflict on the origin of these pores; whether it should stem from an effect due to the physical/mechanical properties of the material or from an effect purely related to the processing parameters. We investigated this problem spanning a range of process parameters for the AISI 316L grade stainless steel. The volume fraction, number density, and size distribution of pores were quantified using X-Ray Computed Tomography (XRCT). Pores formed both at the interface between adjacent layers and within the bulk of the layer. They were systematically sensitive to both the powder material composition and process parameters.

Introduction

Laser-assisted powder deposition, such as Laser Engineered Net Shaping (LENS), is a direct-metal rapid prototyping process, in which metallic powder delivered by the nozzles is melted by the laser beam [1-2]. By moving the substrate or the laser beam, the structure can be built line by line into a wide variety of complex geometries. The LENS process produces a very small heat-affected zone (HAZ) and high cooling rates (> 10^3 °C/s). However, unless a careful tuning of the process parameters is performed, large pores can systematically form either at the interface separating two adjacent layers or within the bulk of the layer [3]. This issue keeps LENS technology from wider acceptance and application in industry.

The interlayer pores elongate along the layer boundaries but with an irregular free surface. It is believed that the presence of these pores can be generally attributed to a discrepancy in the temperature distribution in the deposited material behind the laser track. Unmelted powder could flow onto the colder underlying layer and cause a discrepancy in the melt pool hydrodynamics. This tendency of pore formation was in fact observed to be reduced by careful adjustment of the process parameters, such as laser power and laser scan speed [4-5]. Another important phenomenon could stem from the mechanical properties of the underlying layer. It was observed that a relatively low ductility of the deposited material correlates with more interlayer porosity [6].

The intralayer pores were observed to systematically take a spherical quasi-state form and to not occur in specific locations related to the microstructure. The intralayer pores are still nearly impossible to control, and the mechanisms of their formation are still not formally understood

[7]. It is possible that the gas dissolved or entrapped in the melt may not have sufficient time to escape to the top of the melt pool due to rapid solidification rates associated with typical laser processing. The possible sources of the enclosed gas include surface contamination, entrainment during turbulent impact of particles into the molten pool, contamination by powder-feed gases, gases contained within the powder particles, or vaporization of high vapor pressure alloy constituents. A recent study suggests that the starting powder with certain critical level of porosity and gas content plays an important role on the intralayer porosity formation [3]. Choi and Chang [8] have statistically analyzed the pore distribution for an AISI H13 tool steel and suggested that the powder mass flow rate is a significant factor to porosity.

In this paper, we study the tendency of pore formation by taking account of the effects of process parameters. AISI 316L austenitic stainless steel was used in this study. The thermal and mechanical behavior and phase transformation for LENS deposited AISI 316L and low carbon alloy steel have been investigated numerically and experimentally in the past [9-15]. The interlayer pores and surrounding matrix were subject to Energy Dispersive X-ray (EDX) Spectroscopy in a Field-Emission Scanning Electron microscope (FE-SEM) in an effort to identify any environmental effect on pore formation. The volume fraction, number density, and size distribution of pores in the samples were analyzed using X-ray Computed Tomography (XRCT).

Experimental procedure

The chemical composition for the AISI 316L steel alloy is Fe-0.03C-16.0Cr-2.0Mn-2.0Mo-14.0Ni-1.0Si-0.0045P-0.03S. The powder was gas atomized, supplied by Carpenter Powder Products (Bridgeville, PA). The nominal powder sizes were -80/+270 mesh (approximately 53 to 173 μm diameter). Cylindrical deposits were manufactured under different process parameters, in an argon atmosphere. Oxygen levels in the chamber were monitored and maintained between 3 and 15 ppm. The process parameters and geometry of the samples are listed in Table 1. Totally 7 samples (C1-C7) were studied and subject to detailed analysis through XRCT. 3 small size samples (C1-C3) and 3 large size samples (C4-C6) were studied. All samples were deposited by LENS 750 system, except for sample C7, which was deposited by LENS 850 system with high oxygen content (>20 ppm) in the chamber.

Table 1. Process parameters and geometry for different samples

Sample #	Laser Power (W)	Laser Speed (mm/s)	Layer Thickness (mm)	Powder Flow Rate (g/min)	Diameter (mm)	Length (mm)
C1	450	14.8	0.38	10	9.52	152.4
C2	450	14.8	0.38	10	9.52	152.4
C3	450	14.8	0.38	10	9.52	152.4
C4	400	17.0	0.38	6	15.2	101.6
C5	400	17.0	0.38	6	15.2	101.6
C6	400	17.0	0.38	6	15.2	101.6
C7*	450	14.8	0.38	10	9.52	152.4

*Sample C7 was deposited by LENS 850 system with high oxygen content (>20 ppm).

X-Ray Computed Tomography (XRCT)

A Phoenix X-ray tomography system was employed for the purpose of measuring the porosity distribution in the LENS material. The system is a dual X-ray source capable with possibility to analyze bulk steels up to 25 mm and bulk aluminum up to 75 mm using a 225 kV microfocus. High magnification with minimum geometrical "unsharpness" can be reached using a 160 kV nanofocus. A defect detail of 1 μm can be resolved provided a small sectioning of the sample. Both X-ray sources generate a divergent beam, and as such, the power and exposure time must be carefully adjusted to minimize the "unsharpness" effects. The detector is a PerklinElmer image intensifier with 400 μm pixel size. In this study, the incident X-ray energy level used was between 200kV and 215kV. The current used was between 40μA and 50μA. The rotational increments were 0.6°. Six hundred two-dimensional projection images were recorded for each sample on a 512 × 512 pixel CCD camera. The spatial resolution of the X-ray tomographic set-up was between 14.0 μm and 16.0 μm per voxel, and the incident beam was filtered with a 0.9 mm thick filament of copper.

Sample Preparation

All samples were produced at the facilities of Optomec Design Co. in Albuquerque, NM. The specimens were separated from the substrate at the base. Areas along the bar height that were to be analyzed by XRCT were machined by a CNC lathe down to smaller dimensions that allowed for better x-ray penetration and higher magnification without substantial geometrical "unsharpness" effects. The machined coupons had a diameter ranging between 3.0 mm and 5.0 mm.

Results and discussion

Pores in the AISI 316L Bar Deposits

The pore distribution in this material was analyzed by means of XRCT in 6 samples with different size. The process parameters for these samples were listed in Table 1. Samples C1, C2, and C3 were relatively small with 9.52 mm (0.375 inch) in diameter and 152.4 mm (6.0 inch) in length. A laser power of 450 W and a laser scan speed of 14.8 mm/s were used to manufacture these samples. Samples C4, C5, and C6 were larger and had 15.2 mm (0.6 inch) in diameter and 101.6 mm (4.0 inch) in length. They were manufactured under a laser power of 400 W and a laser scan speed of 17.0 mm/s. The oxygen level in the chamber was maintained below 3.3 ppm.

In this investigation, we performed 3-D reconstructions of acquired 2-D data and numerical calculations of the size and spatial distribution of pores. The XRCT and associated defect analysis software permitted discrimination between different pore shapes. Figure 1 shows the 3D-rendered perspective of quasi-steady state pores that could be exclusively attributed to the gas entrapped during deposition. The pores are represented with red spots within a representative central portion of the sample, i.e. 3-8 mm in length and 3-5 mm in diameter. Samples C1-C5 show similar porosity distribution and the typical result is shown in Figure 1(b) for sample C1. Figure 1(c) shows the porosity distribution for sample C6, which has the same process parameters and geometry as sample C4 and C5. However, the volume fraction of pores in sample C6 is much larger than those in samples C4 and C5. This may be caused by the instability of metal powder flow. The variations in powder mass flow at the nozzle due to irregularly shaped or poorly flowing powder may cause the formation of gas porosity [6]. The complex interaction between metallic powder, delivery gas, and laser can contribute to the formation of pores. Well controlled and stable powder flow can be critical to reduce the gas pores.

Image analysis software was used to analyze the size, shape, and distribution of pores within the samples. The size of each pore was determined by the equivalent diameter of the pore, d , which is defined as the diameter of a sphere giving the same volume as that measured, and is given by:

$$d = 2 \times \sqrt[3]{\frac{3V}{4\pi}} \tag{1}$$

where V is the measured volume of the pore.

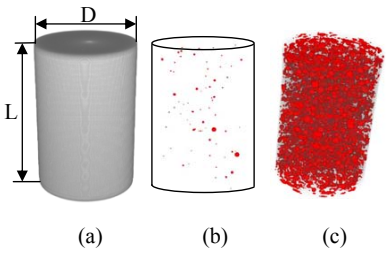

Figure 1. XRCT for LENS samples. (a) Geometry of sample (L=3~8 mm, D=3~5 mm, depends on specimens), (b) C1, (c) C6.

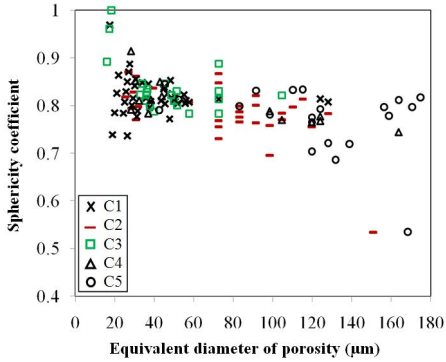

Figure 2. Distribution of calculated sphericity coefficient plotted as a function of the calculated equivalent diameter of porosity for each sample.

The number of pores, largest pore diameter, average pore diameter, volume fraction, number density of pores, and total volume of material were obtained and summarized in Table 2. The average size of pores was in the range of 35 ~ 122 μm. The maximum size of the pores reached 183 μm. The volume fraction of the pores ranged between 0.005% and 0.022%.

Table 2. Quantitative data obtained with X-ray computed tomography on the size and distribution of porosity in the samples.

#	Number of pores	Largest pore diameter (mm)	Average pore diameter (mm)	Volume fraction of porosity (%)	Number density of pores (mm^{-3})	Total volume of material (mm^3)
C1	72	0.124	0.035	0.013	2.315	31.10
C2	40	0.15	0.068	0.016	0.524	76.26
C3	27	0.105	0.046	0.022	2.544	10.61
C4	15	0.163	0.070	0.005	0.110	131.93
C5	22	0.183	0.122	0.017	0.132	166.04

The shape of each pore was characterized by the sphericity coefficient λ, which indicates resemblance of the pore to a perfect sphere and is given according to reference [16] by:

$$\lambda = \sqrt[6]{\frac{36\pi V^2}{S^3}} \tag{2}$$

where S is the surface area of the pore. If λ=1, the pore is perfectly spherical. The coefficient λ, decreases as the shape of the pore becomes less spherical. Figure 2 shows λ plotted against d for all the pores located in the samples. The results indicated that smaller values of λ correlated with larger pores, which probably reveals a coalescence phenomenon. However, the average sphericity did not drop below 0.8, which evidenced that the bulk pores corresponded to gas pores.

Interlayer Porosity due to Unmelted Powder and Oxidation

The interlayer pore distribution was investigated for sample C7 by means of XRCT. This sample was deposited by the LENS 850 system at Optomec. The process parameters of the sample C7, as reported in Table 1, were the same as for the small bars made of AISI 316L (C1, C2, and C3). Figure 3 displays an exclusive 3D rendered perspective of pores in a region between two adjacent layers. The pores appeared in form of large clusters with irregular shapes. The coalescence was significantly more important at the interface between adjacent layers which gave an elongated appearance of the pore clusters. This phenomenon may be due to an oxidation effect since the oxygen level was relatively higher in the chamber of this machine. In fact, surface oxides may most likely remain in solid-state in the melting pool, and as such, upset the wetting mechanisms of adjacent layers. Also the thermal strain incompatibility may directly induce voids. Thus, pore formation would be more favored in these regions.

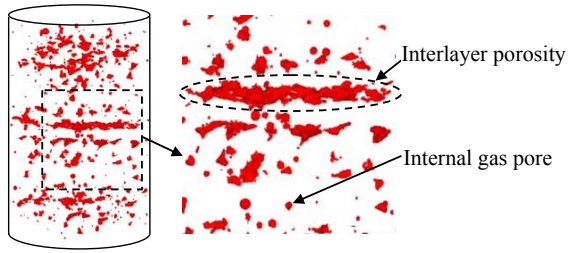

Figure 3. Sample C7 from LENS 850 system shows both interlayer pores and internal gas pores.

The chemical compositions of two interlayer pores for the sample C7 were analyzed using EDX. Figure 4 shows FE-SEM micrographs together with the results of chemical analyses. It can be seen that the pore formation was partially due to unmelted powder that flowed onto the underlying layer, as shown in Figure 4(c). The areas surrounding the pores were analyzed by EDX and a typical peak intensity graph is given in Figure 4(d). The semi-quantitative fractions at each analyzed location in Figure 4(b) are given in Table 3. The results indicated that oxygen content inside the defect; i.e. location B of Figure 4(b) was approximately 7.09wt% (weight fraction), which is much higher than that in location A and C; i.e. 3.24wt% and 2.80wt%, respectively. The compositions of Si and Mn in location B were 4.3 wt%, and 3.1 wt%,

respectively, which were also much higher than other locations far from the interface. This indicates the presence of SiO_2 and MnO close to the interface between adjacent layers delineating noticeable oxidation reactions. These results point to melting discrepancies and oxidation as two interactive mechanisms at the origin of the more substantial pore formation and coalescence at the interfaces between adjacent layers. Table 4 shows the elemental analysis at each analyzed location in Figure 4(c). Oxygen content has no obvious difference at different locations, i.e. 3.13wt%, 4.26wt%, and 3.18wt% in location A, B, and C of Figure 4(c), respectively.

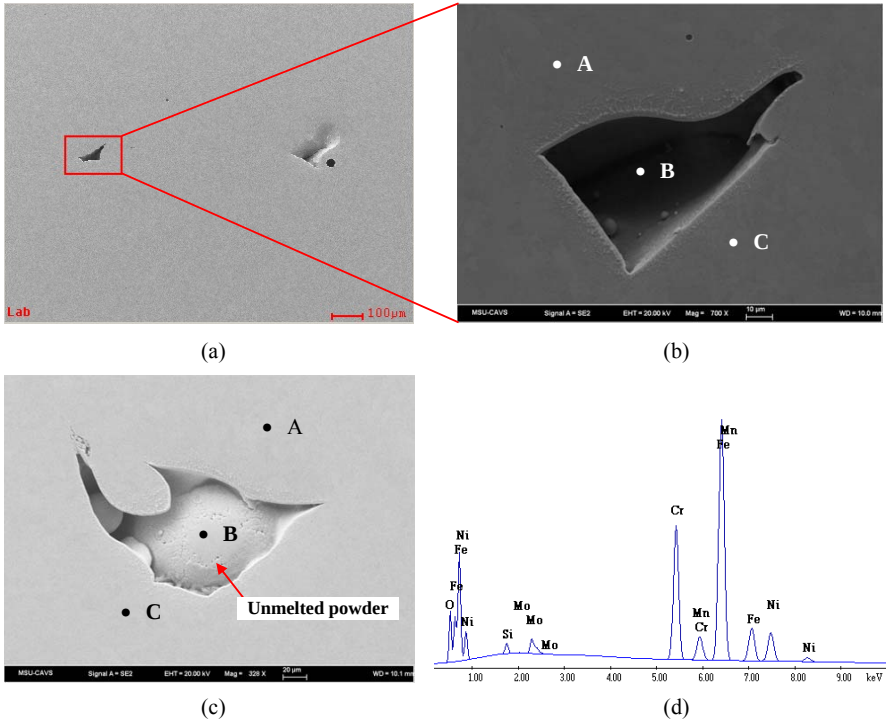

Figure 4 - (a) SEM image of LENS deposited AISI 316L sample C7; (b) high magnification (700x) view of interlayer porosity; (c) SEM image shows the unmelted powder in the interlayer porosity; (d) EDX analysis of the defect, showing the presence of oxygen.

Table 3. Elemental analysis (% weight) by EDX for Figure 4(b).

	O	Si	Mo	Cr	Mn	Fe	Ni
A	3.24	0.8	2.42	20.39	1.44	61.18	10.54
B	7.09	4.3	2.33	22.27	3.1	52.79	8.13
C	2.80	0.81	2.65	20.32	1.15	61.04	11.24
Nominal	-	1.0	2-3	16-18	2.0	Bal.	10-14

Table 4. Elemental analysis (% weight) by EDX for Figure 4(c).

	O	Si	Mo	Cr	Mn	Fe	Ni
A	3.13	0.97	2.52	20.81	1.39	60.29	10.90
B	4.26	0.84	2.72	20.33	1.66	59.13	11.06
C	3.18	0.81	2.22	20.34	1.75	60.56	11.14
Nominal	-	1.0	2-3	16-18	2.0	Bal.	10-14

Conclusions

Pore formation in LENS deposits was studied in cylindrical bars using X-Ray Computed Tomography, FE-SEM and EDX. Interlayer pores appear to correlate with higher oxidation kinetics and unmelted powders. Intralayer pores correlate with the stability of powder flow and the interaction between the metallic powder, delivery gas, and laser power. Well controlled and stable powder flow can be critical to reduce the gas pores.

Acknowledgements

The authors appreciate the sponsorship of the U.S. Army TACOM and the Center for Advanced Vehicular Systems (CAVS) of Mississippi State University. The assistance of Jim Bullen in Optomec Design Co. in fabricating the deposits is also much appreciated.

References

[1] G.K. Lewis, and E. Schlienger, "Practical Considerations and Capabilities for Laser Assisted Direct Metal Deposition," *Materials & Design*, Vol. 21, n4, 2000, pp. 417-423.

[2] M.L. Griffith, M.T. Ensz, J.D. Puskar, C.V. Robino, J.A. Brooks, J.A. Philliber, J.E. Smugeresky, W.H. Hofmeister, "Understanding the Microstructure and Properties of Components Fabricated by Laser Engineered Net Shaping (LENS)", Materials Research Society, Vol. 625, 2000, pp. 9-20.

[3] D.F. Susan, J.D. Puskar, J.A. Brooks, C.V. Robino, "Quantitative Characterization of Porosity in Stainless Steel LENS Powders and Deposits," *Materials Characterization*, Vol. 57, n1, 2006, pp. 36-43.

[4] L. Wang, and S.D. Felicelli, "Process Modeling in Laser Deposition of Multilayer SS410 Steel," *Journal of Manufacturing Science and Engineering*, Vol. 129, No. 6, 2007, pp. 1028-1034.

[5] P.A. Kobryn, E.H. Moore, S.L. Semiatin, "The Effect of Laser Power and Traverse Speed on Microstructure, Porosity, and Build Height in Laser-deposited Ti-6Al-4V," *Scripta Materialia*, Vol. 43, n4, 2000, pp. 299-305.

[6] H.C. Groh III, "Development of Laser Fabricated Ti-6Al-4V," NASA Report, NASA/TM-2006-214256, Glenn Research Center, Cleveland, OH.

[7] J.E. Smugeresky, D.D. Gill, C.J. Atwood, "New low cost material development technique for advancing rapid prototyping manufacturing technology," Sandia Report, SAND2007-7832, 2007, Sandia National Laboratory, Albuquerque, NM.

[8] J. Choi, and Y. Chang, "Characteristics of Laser Aided Direct Metal/Material Deposition Process for Tool Steel," *International Journal of Machine Tools & Manufacturing*, Vol. 45, 2005, pp. 597-607.

[9] H. Yin, L. Wang, and S.D. Felicelli, "Comparison of 2D and 3D Thermal Models of the LENS® Process," ASME *Journal of Heat Transfer*, Vol. 130, No. 10, 2008, pp. 102101-1-7.

[10] L. Wang, S.D. Felicelli, Y. Gooroochurn, P.T. Wang, M.F. Horstemeyer, "Optimization of the LENS® Process for Steady Molten Pool Size," *Materials Science and Engineering A*, Vol. 474, 2008, pp. 148-156.
[11] L. Wang, and S.D. Felicelli, "Analysis of Thermal Phenomena in LENS™ Deposition," *Materials Science and Engineering A*, Vol. 435-436, 2006, pp. 625-631.
[12] L. Wang, S.D. Felicelli, J.E. Craig, "Experimental and Numerical Study of the LENS Rapid Fabrication Process," *Journal of Manufacturing Science and Engineering* (in press).
[13] L. Wang, S.D. Felicelli, and P. Pratt, "Residual Stresses in LENS-deposited AISI 410 Stainless Steel Plates," *Materials Science and Engineering A*, Vol. 496, 2008, pp. 234-241.
[14] P. Pratt, S.D. Felicelli, L. Wang, and C.R. Hubbard, "Residual Stress Measurement of LENS AISI 410 Thin Plates via Neutron Diffraction," *Metallurgical and Materials Transactions A* (in press)
[15] H. El Kadiri, L. Wang, M.F. Horstemeyer, R. Yassar, Y. Shahbazian, S.D. Felicelli, P.T. Wang, "Phase Transformations in Low-alloy Steel Laser Deposits," *Materials Science and Engineering A*, Vol. 494, 2008, pp. 10-20.
[16] J.P. Weiler, J.T. Wood, R.J. Klassen, E. Maire, R. Berkmortel, G. Wang, "Relationship between Internal Porosity and Fracture Strength of Die-cast Magnesium AM60B Alloy," *Materials Science and Engineering A*, Vol. 395, n1-2, 2005, pp. 315-322.